ELECTROCHEMISTRY

Upgrading traditional liquid electrolyte via in situ gelation for future lithium metal batteries

Feng-Quan Liu[1]*, Wen-Peng Wang[2,3]*, Ya-Xia Yin[2,3], Shuai-Feng Zhang[2,3], Ji-Lei Shi[2,3], Lu Wang[1], Xu-Dong Zhang[2,3], Yue Zheng[1], Jian-Jun Zhou[1], Lin Li[1†], Yu-Guo Guo[2,3†]

High-energy lithium metal batteries (LMBs) are expected to play important roles in the next-generation energy storage systems. However, the uncontrolled Li dendrite growth in liquid electrolytes still impedes LMBs from authentic commercialization. Upgrading the traditional electrolyte system from liquid to solid and quasi-solid has therefore become a key issue for prospective LMBs. From this premise, it is particularly urgent to exploit facile strategies to accomplish this goal. We report that commercialized liquid electrolyte can be easily converted into a novel quasi-solid gel polymer electrolyte (GPE) via a simple and efficient in situ gelation strategy, which, in essence, is to use $LiPF_6$ to induce the cationic polymerization of the ether-based 1,3-dioxolane and 1,2-dimethoxyethane liquid electrolyte under ambient temperature. The newly developed GPE exhibits elevated protective effects on Li anodes and has universality for diversified cathodes including but not restricted to sulfur, olivine-type $LiFePO_4$, and layered $LiNi_{0.6}Co_{0.2}Mn_{0.2}O_2$, revealing tremendous potential in promoting the large-scale application of future LMBs.

INTRODUCTION

Rapid expansion of large-scale electric facilities represented by electric vehicles, unmanned planes, and smart electrical grids is witnessed during the past few years (1–3). At the same time, the unprecedented electric energy consumption in modern society has profoundly influenced the prospect of lithium ion batteries (LIBs), where high-energy density is becoming an authentic demand for the days to come (4, 5). Lithium metal batteries (LMBs) consisting of lithium (Li) anodes (3860 mAh g^{-1}) (6, 7), high-energy cathodes (8–10), and stable electrolytes (11, 12) are among the most motivating research territories of lithium secondary batteries (13), but it is also acknowledged that the practical application of LMBs is seriously impeded by uncontrolled Li dendrites and pulverization under liquid electrolytes (LEs) commonly used in LIBs (14, 15). Tremendous efforts have been dedicated through many approaches to overcome the above challenges (16–19), among which the exploration of safe and stable electrolytes with compatibility to metallic Li is particularly critical and indispensable (20).

Today research on gel polymer electrolytes (GPEs) and solid polymer electrolytes (SPEs) is receiving extensive interest (16, 21, 22). As the electrolytes for LMBs, they are featured with superior stabilities toward Li anodes over traditional LEs, but the interfacial problems of GPEs and SPEs within integrated batteries, especially the separation between cathode materials and electrolytes, need to be further resolved. Although in situ polymerization has been proved by numerous studies to be the effective approach to synthesize GPEs and SPEs with compatible interfaces, most of the in situ polymerization strategies used now are derived from free radical theory that requires the presence of extra nonelectrolytic monomers, initi-

ators, and special conditions such as high temperature (22–24). There is still a lack of productive strategies that can take advantage of the conventional materials for commercialized electrolytes without impurity introduction and is meanwhile implementable under moderate external conditions. It is trustworthy that with such a strategy explored and applied in the battery industries, the general commercialization of LMBs based on GPEs and SPEs will be with considerable feasibility.

Herein, a new strategy is crafted to convert traditional ether-based 1,3-dioxolane (DOL) and 1,2-dimethoxyethane (DME) LEs into a novel quasi-solid GPE simply with the addition of commercial lithium hexafluorophosphate ($LiPF_6$). The intriguing chemistry of cationic ring-opening polymerization between $LiPF_6$ and DOL is for the first time unearthed and used in Li secondary battery systems. Compared to most of the commonly used in situ gelation routines, this strategy is designed with incomparable advantages including commercialized materials, free of impurities, and moderate conditions. To the best of our knowledge, it is one of the easiest methods to in situ fabricate polymer-based electrolytes. Derived from the conventional electrolyte system but with superior compatibility toward Li anodes, the GPE exhibits enormous potential as a reliable electrolyte for the next-generation LMBs. In this premise, this novel GPE is successfully applied into a series of LMBs with the cathodes of sulfur, $LiFePO_4$, and $LiNi_{0.6}Co_{0.2}Mn_{0.2}O_2$ (NCM$_{622}$), exhibiting universality and encouraging commercialization prospects.

RESULTS

Gelation mechanism of GPE

The in situ gelation process and its mechanism are demonstrated in Fig. 1A. A liquid precursor obtained by mixing DOL/DME LE with a certain amount of $LiPF_6$ is, in advance, injected into the battery. As revealed in fig. S1 and movie S1, the precursor solution exhibits favorable wettability toward battery components that is comparable with the LE. In addition, the subsequent in situ gelation under ambient conditions forms a new quasi-solid GPE to fulfill the integrated battery. The chemical mechanism involved can be summed up as the
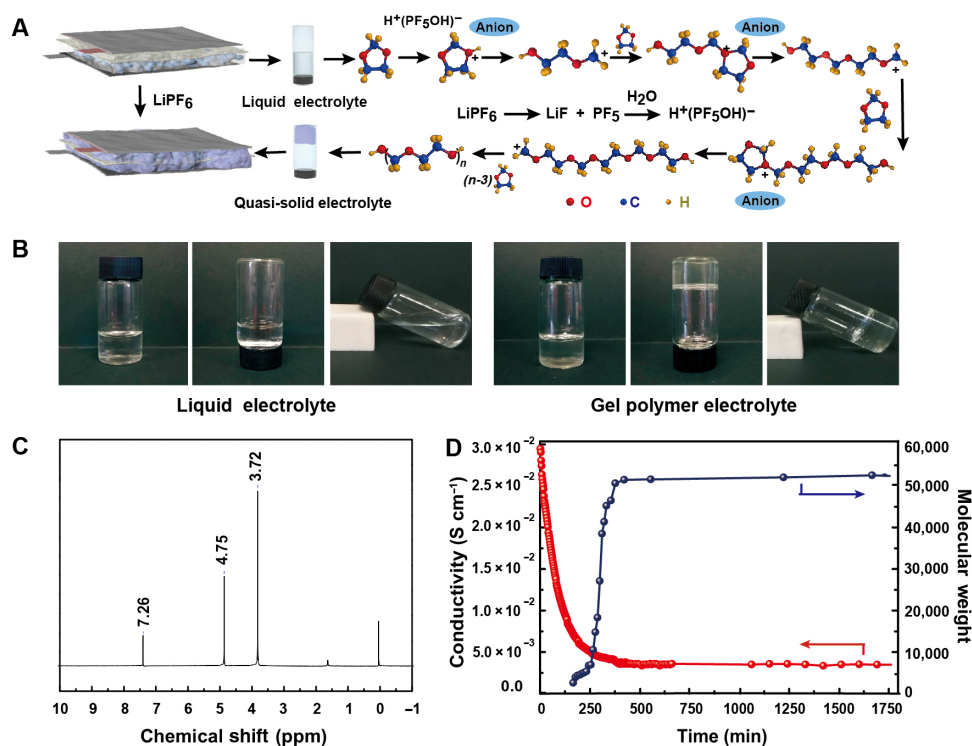
Fig. 1. Mechanism, structure, and characterization of GPE. (**A**) Schematic model of the polymerization mechanism of DOL induced by LiPF$_6$. (**B**) Optical photographs of LE and GPE. (**C**) ^{1}H NMR spectrum of PDXL. Photo credit: Feng-Quan Liu, Beijing Normal University. (**D**) Variation processes of molecular weight (blue dotted line) and ionic conductivity (red dotted line) during gelation process.

cationic-induced DOL ring-opening polymerization with LiPF$_6$ serving as the special "initiator reservoir." It is worth mentioning that the concentration of LiPF$_6$ is selected with a relatively high value, which ensures that, without external heating conditions, the dissolution heat of LiPF$_6$ is sufficient to promote its partial decomposition and releasing a small amount of gaseous phosphorus pentafluoride (PF$_5$), which has been detected with the gas chromatography–mass spectrometry (GC-MS) analysis (fig. S2). PF$_5$ is known as a strong Lewis acid that is also the critical initiator for polymerization (fig. S3) (*22*, *25*), which enables the polymerization to proceed smoothly under room temperature. Namely, in the precursor solution, PF$_5$ combines trace water [12 parts per million (ppm)] to form H$^+$(PF$_5$OH)$^-$, which induces DOL monomers to convert into the reactive second oxonium ions via fast protonation, and the repetitious interposition of DOL monomers into the oxonium ions leads to polymer chain growth. As the polymer grows to a certain degree, trace H$_2$O would attack the oxonium ions and terminate the current chain growth with a nucleophilic substitution (fig. S4). High–molecular weight linear-chain polymer polydioxolane (PDXL) is acquired. Consequently, the integrated homogeneous GPE is eventually established via the combination of the polymer framework (PDXL) with liquid-phase DME. A simulation experiment is executed to enlarge and visualize the microreactions described above, and the reliability of mechanism is confirmed (fig. S5). The optical photographs in Fig. 1B macroscopically demonstrate the gelation evolution where the original flowable liquid solution of DOL/DME LE and LiPF$_6$ turns into a gelatinous electrolyte with immovable and stretchy characteristics, indicating that polymerization has taken place within the electrolyte. Furthermore, both the precursor solu-

tion and GPE remain uniform and transparent as observed, implying that the generation of the lithium fluoride (LiF) from LiPF$_6$ decomposition is too little to be visible, whereas it could still be identified from the x-ray photoelectron spectroscopy (XPS) spectrum of the GPE presented in fig. S6.

To elucidate the structure details of the product, we purified GPE to remove liquid phase and lithium salts leaving only the PDXL. We weighed the acquired PDXL and calculated the polymerization conversion rate of monomer DOL to be as high as 91.0% (table S1). The PDXL chloroform solution is measured by ^{1}H nuclear magnetic resonance (^{1}H NMR; Fig. 1C), in which the chemical shift at 3.72 ppm is assigned to the H on group –O–CH$_2$–CH$_2$–O– and 4.75 ppm represents for group –O–CH$_2$–O–. The integral area ratio of 2:1 indicates the same quantity ratio of the above groups, matching well with the structure of –CH$_2$–O–CH$_2$–CH$_2$–O– as the repeating unit (*26*, *27*). The ^{13}C NMR (fig. S7) and Fourier transform infrared (FTIR; fig. S8) spectra are also obtained to further support the structure conjecture, and the results are consistent with the ^{1}H NMR spectrum.

The gelation process is traced by taking samples from the reactive solution to measure the molecular weight (M_n) and ionic conductivity of the electrolyte seen in fig. S9 and integrated in Fig. 1D. The M_n and ionic conductivity change in opposite regulations with the curve extensions, consistent with the reaction characteristics of cationic polymerization (*25*). This situation suggests that the originally high ion conductivity of electrolyte will decrease originating from the growth of polymer chains. After placement for 10 hours, the M_n reaches ~52,000 (based on polystyrene standard substance), and from almost the same time, the ionic conductivity of the

GPE stabilizes at about 3.8×10^{-3} S cm^{-1}. The high ionic conductivity can be attributed to the unique gelation strategy by transforming part of the original liquid phase (DOL) into solid (PDXL). The framework of PDXL with an ether bond–rich linear chain structure exhibits prominent ability to deliver Li ion (Li$^+$), which has already been investigated in polymers with similar structures such as polyethylene oxide (28, 29). The transport resistance within GPE is tremendously reduced by the DME liquid phase that combines with the PDXL framework as a plasticizer, which exhibits a significant influence on the ion conductivity of the GPE as demonstrated in fig. S10 and table S2. Moreover, it is believed that the GPE derived from the combination of stable polymer framework and liquid DME has much lower volatilization, which is measured to be only one-sixth of the pristine LE (fig. S11). Meanwhile, the melting point of polymer framework can reach 60°C, and the GPE consequently shows fine tolerance and reversibility toward the temperature variation during battery formation, as presented in fig. S12.

Protective effect on Li metal anodes

We assembled symmetrical Li|Li cells with a GPE and a conventional DOL/DME LE to investigate the stability of Li during cycling. Both Li|Li cells are first charged and discharged under a current density of 0.5 mA cm^{-2} for the area capacity of 1.0 mAh cm^{-2}. As demonstrated in Fig. 2A, the charge and discharge of Li|Li battery with GPE can proceed under a significantly low overpotential that is about 20 mV after the first few cycles of activation. Even after the battery is cycled for approximately 800 hours, the voltage polarization still remains less than 25 mV, exhibiting remarkably stable Li deposition and dissolution behaviors. For the battery with LE, apart from the visibly elevated initial voltage polarization compared to GPE, the continuously increasing overpotential also implies the nonuniform Li plating/stripping that is exacerbating upon cycling. Thereafter, another test is implemented where the current density is fixed at a larger value of 1.0 mA cm^{-2} for 1.0 mAh cm^{-2} (Fig. 2B), and it is remarkable to see that the cycling behavior of battery using GPE can still remain stable for more than 400 hours without obvious voltage polarization variation. On the contrary, the battery with LE undergoes similar polarization enlargement during cycling.

The morphologies of Li are observed after cycling under 1.0 mA cm^{-2}. A smooth surface with only a few sporadic coarse sites is maintained for the Li cycled within the GPE (Fig. 2C), where Li dendrites are not shown after cycling. Meanwhile, the cross-sectional image (Fig. 2D) further demonstrates that no pulverization layer is formed. In sharp contrast, the cycling within LE leaves Li with a predominantly pulverized rough surface (Fig. 2E). The higher magnification confirms the existence of Li dendrites with the typical protruding structure (Fig. 2E, inset), and it could therefore be concluded that the uncontrolled growth of dendrites has resulted in the pulverization of Li surface. Furthermore, the cross-sectional image (Fig. 2F) reveals that the pulverization layer has eroded the Li foil to a depth of more than 50 μm. From these results, it can be implied that the instability of Li|Li batteries with LE during cycling is stemmed from the dendrite growth and the consequent pulverization that causes continuous loss of reactive Li. Compared to LE, the GPE has improved interfacial compatibility with Li anodes, and the confinement of a polymer framework to the liquid phase guarantees less contact between a Li surface and reactive electrolyte components, which effectively reduces the interfacial reactions and promotes the even dispersion of Li$^+$ on the Li surface (30), leading

to an impressive capability to suppress dendrite growth and maintain stable cycling.

Figure S13 further presents the Li-Cu battery tests with GPE and LE, respectively. It is demonstrated by fig. S13A that, without any additives, the initial Coulombic efficiency of the Li-Cu battery with GPE attains 90% at 1 mA cm^{-2}. The efficiency after several cycles reaches above 95%, which can remain stable for at least 100 cycles without obvious decline (fig. S13B). As a comparison, the Li-Cu battery with LE shows a relative low first-cycle Coulombic efficiency of 81%. Although it can also reach beyond 90% for a few cycles, an integral decline evidently exhibits after 20 cycles, which could be attributed to the repetitive breakage and repair of the solid electrolyte interphase (SEI) layer during Li plating/stripping originating from a more severe corrosion of Li anodes in LE. Furthermore, specific cycles of charging and discharging are demonstrated. It is obvious that the curves of the Li-Cu battery with GPE (fig. S13C) can maintain stable overpotential without evident polarization increment. As for the Li-Cu battery with LE presented in fig. S13D, a remarkably enlarged overpotential is observed from 30 mV in the 10th cycle toward 70 mV in the 50th cycle. These data suggest that replacing LE with GPE could help maintain a more stable SEI layer and higher reversibility of Li plating/stripping reaction.

Li-S batteries with GPE

The Li-S batteries having high-energy densities are considered promising candidates for future LMBs. However, in the conventional LE systems, the cycle performance of Li-S batteries has long been affected by severe polysulfide shuttling and the resultant loss of electrochemical active species. Since the GPE could still be regarded as an ether-based electrolyte with a unique quasi-solid existence form, it is the seamless alternative to traditional LE for Li-S batteries with efficacious restriction to polysulfide diffusion and the consequent "shuttle effect." The GPE is introduced into the Li-S battery through in situ polymerization with a sufficiently infiltrating precursor solution into a sulfur electrode as illustrated in Fig. 3A. After polymerization, we disassembled the battery for scanning electron microscopy (SEM) observation. The originally exposed cathode and separator (Fig. 3, B and C) are evenly covered by GPE (Fig. 3, D and E), and it is notable that the coverage is not only restricted to the surface but also inside the cathode (fig. S14). Such an in situ polymerization process would drastically reduce the contact resistance between cathode materials and the electrolyte and realize the rapid transmission of Li$^+$. Significantly, the effect of polymer framework as blockage for polysulfide migration is attested by the permeation test in Fig. 3F. In this simulation experiment, the polysulfides scarcely exhibit any infiltration in GPE even after 48 hours of placement. On the contrary, DOL/DME LE shows no resistance to the diffusion of polysulfides. As further verification, we disassembled Li-S batteries with GPE and LE after 50 cycles of charge/discharge at 0.5 C. It is obvious that the separator in LE turns yellow, while the other one soaked with GPE stays almost in its original color (Fig. 3G), which can be a piece of evidence that polysulfides are sealed within the chamber of the cathode by an in situ formed polymer framework.

The charge/discharge curves of both GPE and LE batteries are presented in Fig. 4 (A and B). Li-S battery with GPE exhibits a high initial discharge capacity of 1010 mAh g^{-1} at the rate of 0.5 C (Fig. 4A) due to the superior ionic conductivity and interfacial affinity of GPE. A capacity of 1039 mAh g^{-1} is further delivered by the
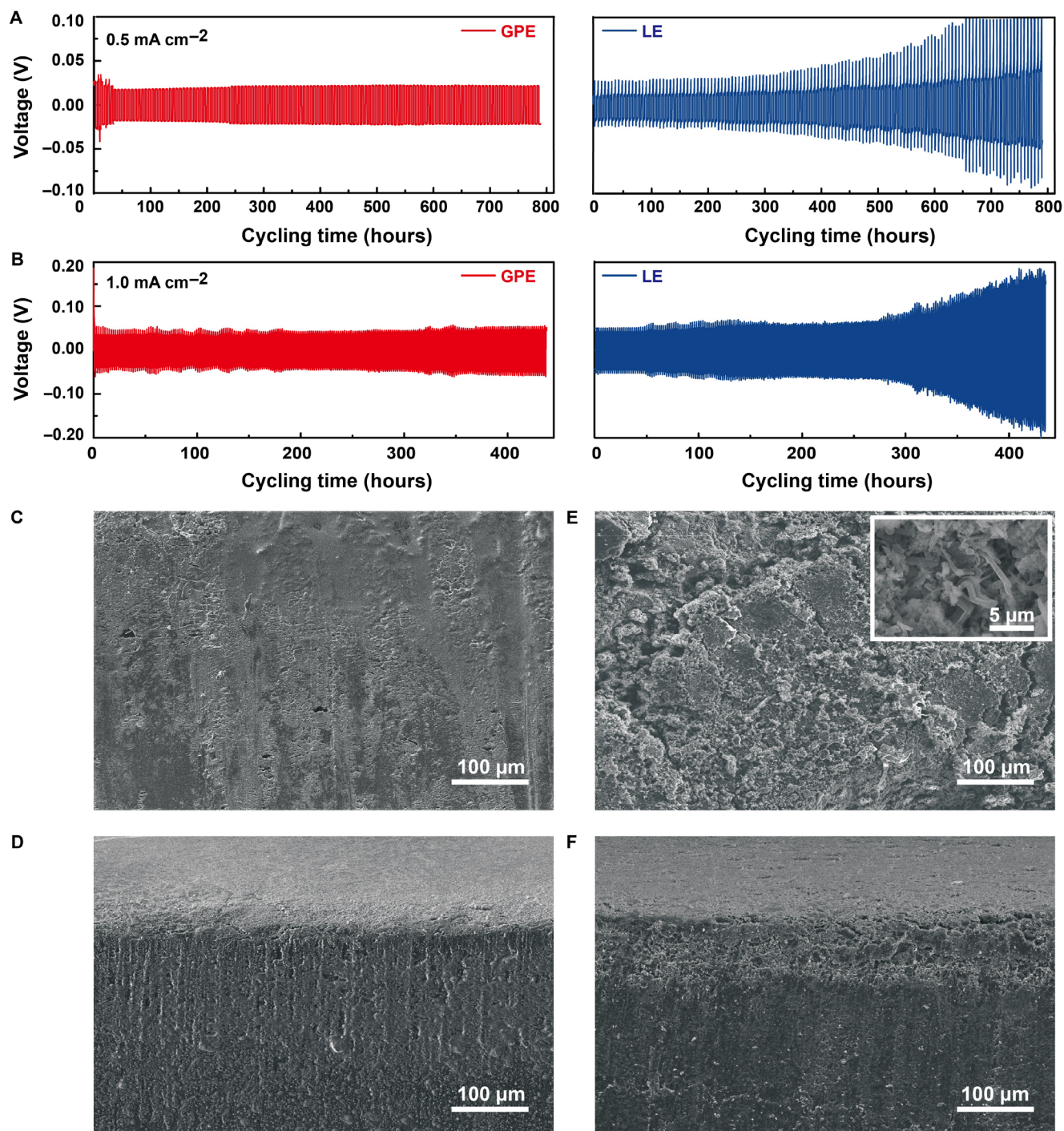
Fig. 2. Electrochemical tests and Li morphologies of Li|Li symmetrical batteries with GPE and LE. Curves of Li|GPE|Li (red lines) and Li|LE|Li (blue lines) symmetrical batteries at room temperature with the current densities of (**A**) 0.5 mA cm^{-2} for 1.0 mAh cm^{-2} and (**B**) 1.0 mA cm^{-2} for 1.0 mAh cm^{-2}. (**C**) Surface morphology and (**D**) cross-sectional morphology of Li anode in GPE system after cycling at 1.0 mA cm^{-2}. (**E**) Surface morphology and (**F**) cross-sectional morphology of Li anode in LE system after cycling at 1.0 mA cm^{-2}.

following charging process with the first-cycle Coulombic efficiency up to 97.2%, which is quite impressive especially in the absence of any consumable additives, indicating the alleviation of shuttle effect from GPE. Another promotion brought by GPE arises from the following several cycles, during which the polysulfides produced en-

counter the in situ confinement of GPE that disables their free diffusion. As a consequence, the second and third charge/discharge curves exhibit scarce fading compared with the first one, while for the Li-S battery with LE (Fig. 4B), the first-cycle Coulombic efficiency is only 78.5% as a proof of shuttle effect, with the capacity
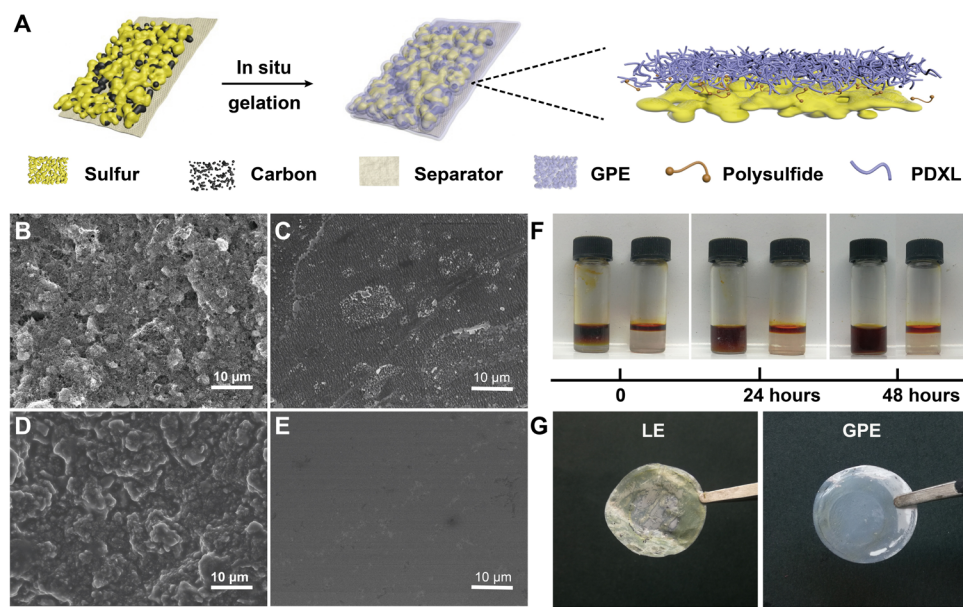
Fig. 3. Schematic diagram, SEM, and optical morphologies of the GPE applied in the Li-S battery. (**A**) Schematic diagram of the in situ polymerization inside the battery system. Surface morphologies of (**B**) KB (Ketjen black)/S composite cathode and (**C**) separator before polymerization. Surface morphologies of (**D**) KB/S composite cathode and (**E**) separator after polymerization. (**F**) Permeation behavior of Li_2S_8 in LE (left) and GPE (right). Photo credit: Wen-Peng Wang, Institute of Chemistry, Chinese Academy of Sciences. (**G**) Optical photographs of separators harvested from the Li-S batteries with LE (left) and GPE (right) after 50 cycles at 0.5 C. Photo credit: Feng-Quan Liu, Beijing Normal University.

fading happening severely in the earliest cycles. Figure 4C depicts that the cyclic voltammogram (CV) profiles of GPE overlap well with each other with two anodic peaks of 2.30 and 2.40 V as well as two cathodic peaks of 2.25 and 2.05 V, which are typical electrochemical peaks of sulfur, indicating mere oxidation and reduction conversions between sulfur and sulfides without side reactions (*31–33*). In comparison, the CV curves of the battery with LE (Fig. 4D) demonstrate the existence of severe shuttle effect, and from the second cycle, a visible shift of oxidation peaks to higher voltage emerges, indicating detrimentally enlarged polarization that will affect the following battery performances.

After 500 cycles at 0.5 C, the capacity of the Li-S battery using GPE remains 741 mAh g^{-1} with an excellent capacity retention of 73.7% (Fig. 4E). As the measurement extends to 1000 cycles, the battery still maintains half of its initial capacity corresponding to the low decay of only 0.05% per cycle. The Coulombic efficiency retains more than 97.0% throughout the total cycling, figuring fine stability against ultralong cycling trial. Comparatively, the Li-S battery with LE undergoes an abrupt capacity decline during the first 300 cycles from 1010 to 370 mAh g^{-1} and is compelled to cycle under a quite low capacity, which, to the end, is only below 200 mAh g^{-1}. The Coulombic efficiency of less than 85.0% during whole cycling implies an ever-present shuttle effect. Upon cycling, we measured the Nyquist profiles of both batteries, from which it can be observed that the internal resistance remains stable in Li-S battery with GPE (fig. S15A). For the battery with LE (fig. S15B), the resistance increases continually, indicating that the soluble polysulfides shuttling recklessly will eventually deposit on the surface of an anode as insoluble and insulated components, which are responsible for the tougher Li$^+$ transport. To further support the results, we investigated the microstructures of Li anodes in Li-S batteries with GPE and LE after 50 cycles at 0.5 C. For Li-S battery with GPE (fig. S15C), the Li surface

after cycling is smooth and free of depositions, while in LE (fig. S15D), a large proportion of Li surface is covered by rough sediments. The feather-like depositions (fig. S15D, inset) are further identified as a series of sulfides derived from the side reactions between lithium polysulfides and Li by XPS characterization (fig. S16), and their accumulation blocks the normal plating and stripping of Li$^+$ (*34*, *35*). It is also noteworthy that the utilization of GPE benefits Li-S battery with higher self-discharge resistance, which is one of the most important properties in practical application (fig. S17). The discharge process of the battery with GPE is interrupted on the 11th cycling, with the cutoff voltage at 2.05 V where the amount of soluble polysulfides is at the highest level (fig. S17, A and B). After 1-week placement, the battery restores its foregoing discharge process and exhibits a capacity decay of only 6% compared to the 10th cycle. Notably, in the subsequent cycles, a minor rise in capacity indicates that the activation process also contributes to the capacity decay, which is reversible; thus, the actual capacity degradation derived from self-discharge is even slighter. In contrast, we conducted the same interruption on the battery with LE in fig. S17 (C and D). The recovered discharge process of Li-S battery with LE rapidly terminates with a capacity of only 350 mAh g^{-1}, representing capacity loss as high as 40% that is irreversible.

Universality of GPE in Li-LiFePO$_4$ and Li-NCM$_{622}$ batteries

In commercialized battery systems, intercalating cathodes olivine-type LiFePO$_4$ and layered NCM$_{622}$ are two of the commonly used materials (*36*). To identify the universality of GPE toward commercialized cathode materials, we assembled a battery of LiFePO$_4$|Li using GPE and cycled at the current rate of 0.5 C (Fig. 5A). The bandgap of only 0.14 V between charge and discharge platforms that is comparable with the battery using LE (fig. S18) implies minor polarization and highlights excellent ion conducting capability
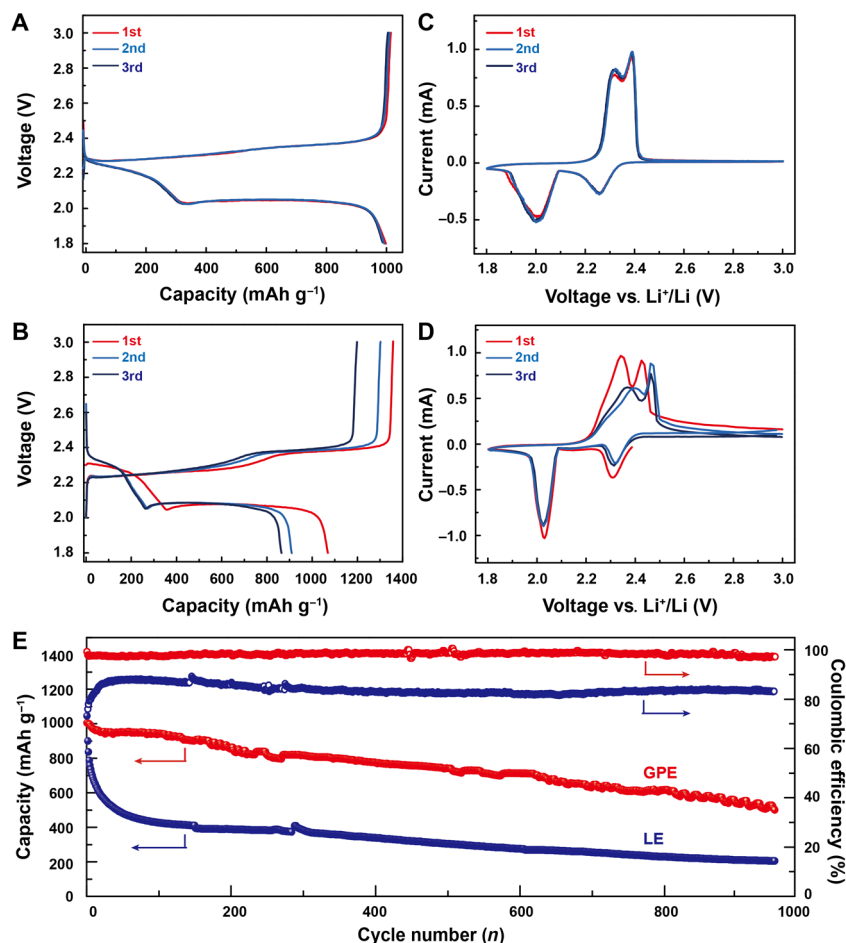
Fig. 4. Electrochemical performances of Li-S batteries with GPE and LE. Charge/discharge curves of Li-S batteries (**A**) with GPE and (**B**) with LE for the first three cycles at the rate of 0.5 C. The CV curves of Li-S batteries (**C**) with GPE and (**D**) with LE for the first three cycles at a scanning rate of 0.05 mV s^{-1}. (**E**) Cycling performance and Coulombic efficiency of the batteries with GPE and LE.

and slight interfacial resistance. Cycling stability is also fairly compared between the LiFePO$_4$|GPE|Li battery and the LiFePO$_4$|LE|Li battery (Fig. 5B). In the final period of cycling at 0.5 C, the LiFePO$_4$|LE|Li battery exhibits a scattered and reduced capacity and Coulombic efficiency, which arise from the efficiency loss of Li anodes. By contrast, the LiFePO$_4$|GPE|Li battery undergoes no obvious fading either in capacity or in Coulombic efficiency, with a capacity retention of 95.6% after 700 cycles and a stable Coulombic efficiency of more than 99.5%, indicating superior interface stability between electrodes and GPE.

Compared to LiFePO$_4$, the charging voltage of which is generally limited at 4.00 V, layered LiNi$_x$Co$_y$Mn$_{1-x-y}$O$_2$ (NCM) with a voltage of up to 4.30 V is considered a more promising cathode material to meet the demand for high-energy LMBs [37]. However, it is well recognized that ether-based DOL/DME LE has seldom taken steps into the territory of layered NCM materials because of its extreme instability and oxidation intention under high voltage. Normally, the DOL/DME LE starts to become unstable when the voltage rises to 4.00 V and undergoes serious decomposition at the voltage of more than 4.20 V (Fig. 6A). This means that, when matching DOL/DME LE with NCM$_{622}$ and selecting a typical cutoff voltage of 4.30 V, the battery suffers a severe overcharging phenomenon (Fig. 6B) attributed

to massive solvent oxidation and decomposition. Theoretically, the instability of liquid-phase DOL/DME to a large extent originates from the DOL with an unstable cyclic structure [38, 39], which implies that, after a ring-opening polymerization process where the cyclic DOL is, in advance, stabilized in the long-chain linear structure, the tolerance of electrolyte toward electrochemical progress under high voltage could be improved. As proof, the linear sweep voltammetry (LSV) curve presented in Fig. 6C demonstrates that there are no obvious decomposition currents of GPE until the voltage reaches 4.60 V. Using a cathode of NCM$_{622}$ to match the GPE with a voltage limitation of 4.30 V can as well achieve normalized charge and discharge behaviors at the rate of 0.1 C without an oxidation-led overcharging phenomenon (Fig. 6D). Notably, the capacity and Coulombic efficiency retention of an NCM$_{622}$|GPE|Li battery for a period of 100 cycles shown in Fig. 6E further prove that these stabilities have endurance toward repetitive charges and discharges.

High flexibility and robust mechanical affordability are also the pursuits referring to commercialized batteries [40]. We assembled a soft packed NCM$_{622}$|GPE|Li battery and tested its ability to power light-emitting diode (LED) lamps under various mechanical deformations. As shown in Fig. 6F, the power delivery exhibits no failure regardless of the shape changes of either bending or even folding.
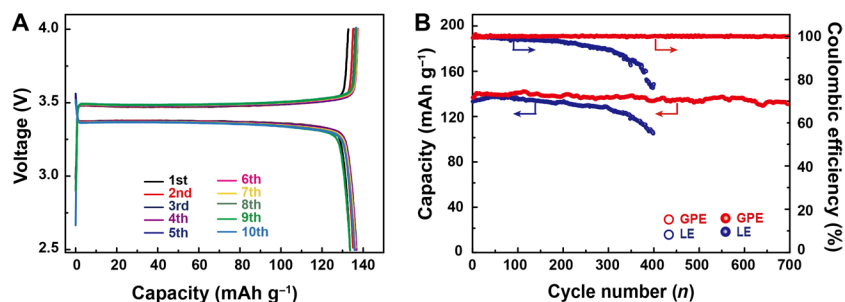
Fig. 5. Electrochemical performances of LiFePO₄|GPE|Li battery and LiFePO₄|LE|Li battery. (**A**) Charge/discharge curves of LiFePO₄|GPE|Li battery. (**B**) Cycling performance and Coulombic efficiency of LiFePO₄|GPE|Li battery and LiFePO₄|LE|Li battery.
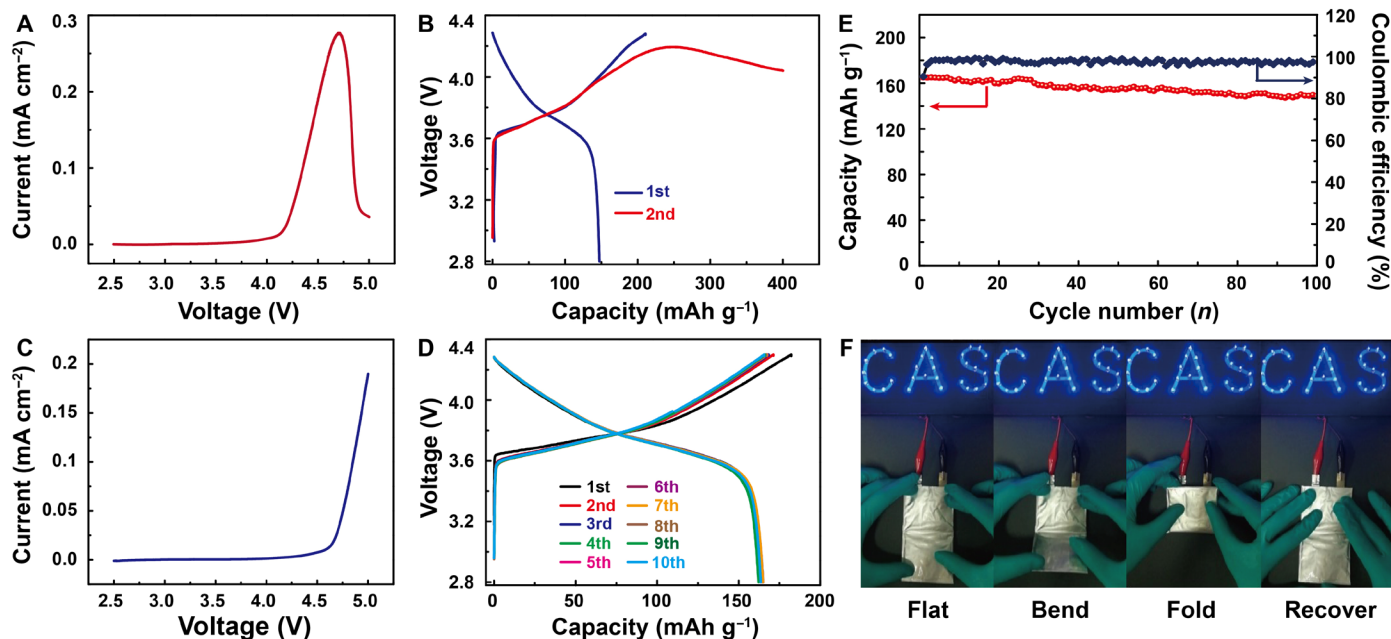

Fig. 6. Electrochemical performances of NCM₆₂₂|GPE|Li battery and NCM₆₂₂|LE|Li battery. LSV curves of (**A**) LE and (**C**) GPE with the voltage range of 2.5 to 5.0 V at room temperature. Charge/discharge curves of (**B**) NCM₆₂₂|LE|Li battery and (**D**) NCM₆₂₂|GPE|Li battery with the voltage range of 2.8 to 4.3 V. (**E**) Cycling performance and Coulombic efficiency of NCM₆₂₂|GPE|Li battery. (**F**) Optical images of LED lamps lighted by flexible NCM₆₂₂|GPE|Li battery under various mechanical deformations. Photo credit: Wen-Peng Wang, Institute of Chemistry, Chinese Academy of Sciences.

This can be attributed to the GPE with much reduced mobility along with higher mechanical strength (fig. S19), which contributes to maintaining stronger and more stable attachment of interfaces, and consequently, the battery demonstrates improved adaptation toward shape transformation.

DISCUSSION

In summary, this study innovatively uses LiPF₆ to induce the in situ gelation of a traditional DOL/DME LE, by which an intriguing quasi-solid GPE is acquired spontaneously under ambient conditions. The novel strategy demonstrated in this work with the mechanism of cationic ring-opening polymerization as its internal motivation is among the most facile and straightforward approaches to fabricate polymer-based gelatinous electrolytes. The as-prepared quasi-solid GPE exhibits effective constraint to the dendrite growth and pulverization of Li anodes, which makes it a promising electrolyte for prospective LMBs. In addition, the GPE is manifested to be universal for diverse LMBs with various superiorities de-

pending on the cathode chemistries. (i) The GPE with efficacious restrictions to polysulfide diffusion and shuttle effect can provide the Li-S battery with high Coulombic efficiency (>97.0% without additives) and outstanding long-cycling capacity retention for at least 1000 cycles with the low decay of 0.05% per cycle. (ii) The utilization of GPE in commercialized LiFePO₄|Li batteries demonstrates excellent stability with the capacity retention up to 95.6% after 700 cycles. (iii) The GPE has an evidently broadened electrochemical stability interval and is capable of matching NCM₆₂₂ for normal and stabilized cycling with a cutoff voltage of 4.30 V, thus breaking the voltage limitations for traditional ether-based electrolytes. The GPE is derived from exactly the most conventional electrolyte materials and with unprecedented adaptability to the packing technologies of current battery systems, hence its application in actual industrializations is quite foreseeable. This study is believed to generate a wider interest in upgrading the traditional electrolyte systems through innovative strategies, which may become a new frontier in the exploration of advanced electrolyte systems for future LMBs.

MATERIALS AND METHODS

Synthesis of GPE

The GPE was prepared by in situ gelation of a precursor solution in a sealed pellucid glass reagent bottle. The precursor solution consisted of 2 M $LiPF_6$ dissolved in a common DOL/DME LE, which contained 1 M lithium bis(trifluoromethanesulfonyl)imide (LiTFSI) in a mixed organic solution of DOL and DME (1:1 , v/v). The precursor solution spontaneously transformed into GPE by standing for a period of time at room temperature. All processes of preparing the GPE were conducted in an Ar-filled glove box.

Separation and purification of PDXL from GPE

PDXL was separated and purified as follows. The GPE was dispersed with absolute ethyl alcohol, and then the mixed solution was centrifuged at 8000 rpm for 5 min. The supernatant fluid was poured out, and lower precipitation was dispersed again with new clean ethanol and centrifuged. The above process was repeated more than five times to separate the white precipitate. The obtained white precipitate was dried by natural volatilization at room temperature to remove redundant ethanol and obtained the isolated polymer named as PDXL.

Preparation of cathodes and fabrication of batteries

Pure sulfur (analytical reagent, Sigma-Aldrich) was mixed with KB according to the quality ratio of 7:3. The mixtures were then sealed in a glass container and heated at 400°C for 20 hours to make sulfur and KB disperse fully and achieve nanoscale sulfur. The KB/S composite was acquired after being naturally cooled to room temperature.

The cathode electrodes for Li-S, Li-LiFePO$_4$, and Li-NCM$_{622}$ batteries were fabricated by respectively mixing the KB/S composite, LiFePO$_4$, and NCM$_{622}$ with Super P and polyvinylidene difluoride binder with a weight ratio of 8:1:1 via N-methyl-2-pyrrolidone as a solvent. The slurries were immobilized on carbon-coated Al foils and dried for 24 hours in a vacuum oven at 60°, 80°, and 80°C, respectively. The sulfur, LiFePO$_4$, and NCM$_{622}$ cathodes were tailored in the diameter of 10 mm with active material loads to be about 1.5, 5.0, and 3.0 mg cm^{-2}.

CR2032-type coin cells were assembled in an Ar-filled glove box (H$_2$O < 0.1 ppm, O$_2$ < 0.1 ppm). The coin cells with GPE were fabricated simply by direct in situ polymerization. The Celgard separator was sandwiched between the cathode and Li foil. The precursor solution was injected into the separator, and the batteries were filled with precursor solution. Subsequently, the assembled batteries were left to stand for a period of time to form GPE completely inside the battery. The comparison coin cells were fabricated by the same route except for the usage of the common LE of 1.0 M LiTFSI in DOL/DME with a volume ratio of 1:1.

Characterizations

The FTIR spectrum of the prepared PDXL was recorded using SHIMADZU IRAffinity-1 in the range of 400 to 4000 cm^{-1} to investigate the functional group of PDXL. ^{1}H NMR and ^{13}C NMR spectra of PDXL were collected on a Bruker AVANCE III 400 MHz with CDCl$_3$ as a deuterated solvent and tetramethylsilane as an internal reference to obtain the structure of PDXL. The thermogravimetric analysis of LiPF$_6$ was measured by an apparatus (Q600 SDT America, TA Instruments) from 25° to 350°C. XPS was explored on the Thermo Scientific ESCALab 250Xi (Thermo Fisher Scientific). An Instron 3366 electronic universal testing machine (Instron Corpo-

ration) was used in mechanical testing. The contact angle measurements were conducted on the Contact Angle Meter (OCA 20, Dataphysics Company). A gel permeation chromatograph (PL-GPC50) was used to measure the molecular weight of the samples with tetrahydrofuran as a solvent and to measure the mobile phase. Contrast experiments on volatilization of GPE and LE were designed as follows: The changes in weight of GPE and LE with the same original weight as time goes on were recorded in an Ar-filled glove box at room temperature. Li$_2$S$_8$ solution (0.2 M) was prepared as follows: Li$_2$S and sulfur were added into a glass transparent reagent bottle with DME in accordance with stoichiometric ratio and mixed uniformly by magnetic stirring until the miscible liquid turns to dark brown. Li$_2$S$_8$ solution (100 μl) was dropped into the bottles, in which GPE and LE had the same volume.

Electrochemical characterizations

The precursor solution of GPE was prepared in a transparent glass bottle, and two stainless steel plates were inserted below the liquid level. The changes in the conductivity of the system, from flexible precursor solution to immobile GPE, were recorded by an electrochemical workstation (Interface 1000E, Gamry Instruments). The conductivity was calculated by the following equation: $G = l/(RS)$, where l is the distance between two stainless steel plates, R is the resistance value, and S is the effective area below the liquid surface. The LSV curves of GPE and LE were obtained by placing the GPE/LE between a stain steel plate and lithium foil at a sweep rate of 1.0 mV s^{-1}. The CVs of batteries with GPE and LE were measured via the electrochemical workstation (Interface 1000E, Gamry Instruments) in the voltage range of 1.8 to 3.0 V at a scanning rate of 0.05 mV s^{-1}. Electrochemical impedance spectra (EIS) of batteries with GPE and LE were tested by the electrochemical workstation (Interface 1000E, Gamry Instruments) in the frequency range of 10^{-1} to 10^5 Hz. The Li|GPE|Li and Li|LE|Li symmetric cells were studied using LAND (LANHE CT2001A) using different current densities. The galvanostatic charge/discharge tests of batteries, including Li-S batteries, Li-LiFePO$_4$ batteries, and Li-NCM$_{622}$ batteries with GPE and LE were examined using the LAND testing system (LANHE CT2001A).

Table S2. Ion conductivity of GPE with various DME content in the precursors.

Movie S1. Contact angle measurement of polymer precursor and LE on cathode substrates.

REFERENCES AND NOTES

1. J.-M. Tarascon, M. Armand, Issues and challenges facing rechargeable lithium batteries. *Nature* **414**, 359–367 (2001).

2. J. Zhi, A. Z. Yazdi, G. Valappil, J. Haime, P. Chen, Artificial solid electrolyte interphase for aqueous lithium energy storage systems. *Sci. Adv.* **3**, e1701010 (2017).

3. Z. Tu, M. J. Zachman, S. Choudhury, S. Wei, L. Ma, Y. Yang, L. F. Kourkoutis, L. A. Archer, Nanoporous hybrid electrolytes for high-energy batteries based on reactive metal anodes. *Adv. Energy Mater.* **7**, 1602367 (2017).

4. K. Yan, Z. Lu, H.-W. Lee, F. Xiong, P.-C. Hsu, Y. Li, J. Zhao, S. Chu, Y. Cui, Selective deposition and stable encapsulation of lithium through heterogeneous seeded growth. *Nat. Energy* **1**, 16010 (2016).

5. W. Zhang, H.-C. Yu, L. Wu, H. Liu, A. Abdellahi, B. Qiu, J. Bai, B. Orvananos, F. C. Strobridge, X. Zhou, Z. Liu, G. Ceder, Y. Zhu, K. Thornton, C. P. Grey, F. Wang, Localized concentration reversal of lithium during intercalation into nanoparticles. *Sci. Adv.* **4**, eaao2608 (2018).

6. J. Zheng, M. H. Engelhard, D. Mei, S. Jiao, B. J. Polzin, J.-G. Zhang, W. Xu, Electrolyte additive enabled fast charging and stable cycling lithium metal batteries. *Nat. Energy* **2**, 17012 (2017).

7. W. Xu, J. Wang, F. Ding, X. Chen, E. Nasybulin, Y. Zhang, J.-G. Zhang, Lithium metal anodes for rechargeable batteries. *Energy Environ. Sci.* **7**, 513–537 (2014).

8. Y.-X. Yin, S. Xin, Y.-G. Guo, L.-J. Wan, Lithium-sulfur batteries: Electrochemistry, materials, and prospects. *Angew. Chem. Int. Ed.* **52**, 13186–13200 (2013).

9. S. Choudhury, C. T.-C. Wan, W. I. Al Sadat, Z. Tu, S. Lau, M. J. Zachman, L. F. Kourkoutis, L. A. Archer, Designer interphases for the lithium-oxygen electrochemical cell. *Sci. Adv.* **3**, e1602809 (2017).

10. G. Zhou, S. Pei, L. Li, D.-W. Wang, S. Wang, K. Huang, L.-C. Yin, F. Li, H.-M. Cheng, A graphene-pure-sulfur sandwich structure for ultrafast, long-life lithium-sulfur batteries. *Adv. Mater.* **26**, 625–631 (2014).

11. M. D. Tikekar, S. Choudhury, Z. Tu, L. A. Archer, Design principles for electrolytes and interfaces for stable lithium-metal batteries. *Nat. Energy* **1**, 16114 (2016).

12. L. Suo, Y.-S. Hu, H. Li, M. Armand, L. Chen, A new class of solvent-in-salt electrolyte for high-energy rechargeable metallic lithium batteries. *Nat. Commun.* **4**, 1481 (2013).

13. K. K. Fu, Y. Gong, B. Liu, Y. Zhu, S. Xu, Y. Yao, W. Luo, C. Wang, S. D. Lacey, J. Dai, Y. Chen, Y. Mo, E. Wachsman, L. Hu, Toward garnet electrolyte-based Li metal batteries: An ultrathin, highly effective, artificial solid-state electrolyte/metallic Li interface. *Sci. Adv.* **3**, e1601659 (2017).

14. Y. Liu, D. Lin, P. Y. Yuen, K. Liu, J. Xie, R. H. Dauskardt, Y. Cui, An artificial solid electrolyte interphase with high Li-ion conductivity, mechanical strength, and flexibility for stable lithium metal anodes. *Adv. Mater.* **29**, 1605531 (2017).

15. H. Ye, S. Xin, Y.-X. Yin, J.-Y. Li, Y.-G. Guo, L.-J. Wan, Stable Li plating/stripping electrochemistry realized by a hybrid Li reservoir in spherical carbon granules with 3D conducting skeletons. *J. Am. Chem. Soc.* **139**, 5916–5922 (2017).

16. M. D. Tikekar, L. A. Archer, D. L. Koch, Stabilizing electrodeposition in elastic solid electrolytes containing immobilized anions. *Sci. Adv.* **2**, e1600320 (2016).

17. J. T. Vaughey, G. Liu, J.-G. Zhang, Stabilizing the surface of lithium metal. *MRS Bull.* **39**, 429–435 (2014).

18. C.-P. Yang, Y.-X. Yin, S.-F. Zhang, N.-W. Li, Y.-G. Guo, Accommodating lithium into 3D current collectors with a submicron skeleton towards long-life lithium metal anodes. *Nat. Commun.* **6**, 8058 (2015).

19. L. Ma, M. S. Kim, L. A. Archer, Stable artificial solid electrolyte interphases for lithium batteries. *Chem. Mater.* **29**, 4181–4189 (2017).

20. L. Hu, K. Xu, Nonflammable electrolyte enhances battery safety. *Proc. Natl. Acad. Sci. U.S.A.* **111**, 3205–3206 (2014).

21. S. Gao, K. Wang, R. Wang, M. Jiang, J. Han, T. Gu, S. Cheng, K. Jiang, Poly(vinylidene fluoride)-based hybrid gel polymer electrolytes for additive-free lithium sulfur batteries. *J. Mater. Chem. A* **5**, 17889–17895 (2017).

22. D. Zhou, Y.-B. He, Q. Cai, X. Qin, B. Li, H. Du, Q.-H. Yang, F. Kang, Investigation of cyano resin-based gel polymer electrolyte: In situ gelation mechanism and electrode–electrolyte interfacial fabrication in lithium-ion battery. *J. Mater. Chem. A* **2**, 20059–20066 (2014).

23. J. Chai, Z. Liu, J. Ma, J. Wang, X. Liu, H. Liu, J. Zhang, G. Cui, L. Chen, In situ generation of poly (vinylene carbonate) based solid electrolyte with interfacial stability for LiCoO₂ lithium batteries. *Adv. Sci.* **4**, 1600377 (2017).

24. M. Liu, D. Zhou, Y.-B. He, Y. Fu, X. Qin, C. Miao, H. Du, B. Li, Q.-H. Yang, Z. Lin, T. S. Zhao, F. Kang, Novel gel polymer electrolyte for high-performance lithium–sulfur batteries. *Nano Energy* **22**, 278–289 (2016).

25. K. Xu, Nonaqueous liquid electrolytes for lithium-based rechargeable batteries. *Chem. Rev.* **104**, 4303–4418 (2004).

26. S. K.-L. Siu, C. Y.-S. Chung, V. W.-W. Yam, Amphiphilic oligo(ethylene glycol)- and poly(ethyleneoxide)-*block*-poly(propylene oxide)-*block*-poly-(ethylene oxide)-containing cyclometalated alkynylgold(III) complexes: From basic photophysics to self-assembly and stimuli-responsive properties. *J. Organomet. Chem.* **845**, 177–188 (2017).

27. R. Ali, A. Farah, Z. Binkhathlan, Development and characterization of methoxy poly (ethylene oxide)-*block*-poly(ε-caprolactone) (PEO-*b*-PCL) micelles as vehicles for the solubilization and delivery of tacrolimus. *Saudi Pharm. J.* **25**, 258–265 (2017).

28. M. Barghamadi, A. S. Best, A. I. Bhatt, A. F. Hollenkamp, M. Musameh, R. J. Rees, T. Rüther, Lithium–sulfur batteries–the solution is in the electrolyte, but is the electrolyte a solution? *Energy Environ. Sci.* **7**, 3902–3920 (2014).

29. Z. Lin, C. Liang, Lithium–sulfur batteries: From liquid to solid cells. *J. Mater. Chem. A* **3**, 936–958 (2015).

30. W. Zhou, S. Wang, Y. Li, S. Xin, A. Manthiram, J. B. Goodenough, Plating a dendrite-free lithium anode with a polymer/ceramic/polymer sandwich electrolyte. *J. Am. Chem. Soc.* **138**, 9385–9388 (2016).

31. G. Xu, A. Kushima, J. Yuan, H. Dou, W. Xue, X. Zhang, X. Yan, J. Li, *Ad hoc* solid electrolyte on acidized carbon nanotube paper improves cycle life of lithium–sulfur batteries. *Energy Environ. Sci.* **10**, 2544–2551 (2017).

32. Z. Zhao, D. Qin, S. Wang, G. Chen, Z. Li, Fabrication of high conductive S/C cathode by sulfur infiltration into hierarchical porous carbon/carbon fiber weave-structured materials via vapor-melting method. *Electrochim. Acta* **127**, 123–131 (2014).

33. J. Guo, Z. Yang, Y. Yu, H. D. Abruña, L. A. Archer, Lithium–sulfur battery cathode enabled by lithium–nitrile interaction. *J. Am. Chem. Soc.* **135**, 763–767 (2013).

34. C. P. Yang, Y.-X. Yin, Y.-G. Guo, L.-J. Wan, Electrochemical (De)Lithiation of 1D sulfur chains in Li–S batteries: A model system study. *J. Am. Chem. Soc.* **137**, 2215–2218 (2015).

35. L. Wang, J. Liu, S. Yuan, Y. Wang, Y. Xia, To mitigate self-discharge of lithium–sulfur batteries by optimizing ionic liquid electrolytes. *Energy Environ. Sci.* **9**, 224–231 (2016).

36. H. Hafiz, K. Suzuki, B. Barbiellini, Y. Orikasa, V. Callewaert, S. Kaprzyk, M. Itou, K. Yamamoto, R. Yamada, Y. Uchimoto, Y. Sakurai, H. Sakurai, A. Bansil, Visualizing redox orbitals and their potentials in advanced lithium-ion battery materials using high-resolution x-ray Compton scattering. *Sci. Adv.* **3**, e1700971 (2017).

37. S. Röser, A. Lerchen, L. Ibing, X. Cao, J. Kasnatscheew, F. Glorius, M. Winter, R. Wagner, Highly effective solid electrolyte interphase-forming electrolyte additive enabling high voltage lithium-ion batteries. *Chem. Mater.* **29**, 7733–7739 (2017).

38. R. Miao, J. Yang, Z. Xu, J. Wang, Y. Nuli, L. Sun, A new ether-based electrolyte for dendrite-free lithium-metal based rechargeable batteries. *Sci. Rep.* **6**, 21771 (2016).

39. H. Zhong, C. Wang, Z. Xu, F. Ding, X. Liu, A novel quasi-solid state electrolyte with highly effective polysulfide diffusion inhibition for lithium-sulfur batteries. *Sci. Rep.* **6**, 25484 (2016).

40. H.-J. Peng, J.-Q. Huang, Q. Zhang, A review of flexible lithium–sulfur and analogous alkali metal–chalcogen rechargeable batteries. *Chem. Soc. Rev.* **46**, 5237–5288 (2017).

Citation: F.-Q. Liu, W.-P. Wang, Y.-X. Yin, S.-F. Zhang, J.-L. Shi, L. Wang, X.-D. Zhang, Y. Zheng, J.-J. Zhou, L. Li, Y.-G. Guo, Upgrading traditional liquid electrolyte via in situ gelation for future lithium metal batteries. *Sci. Adv.* **4**, eaat5383 (2018).